



Cite this: *CrystEngComm*, 2016, **18**,  
496

## Enhanced photoelectronic properties of single crystal $\text{TiO}_2$ nanosheet array films by selective deposition of CdS nanoparticles on their $\{101\}$ facets

Lei Yang,<sup>a,b</sup> Haiyan Jiang,<sup>c</sup> Weihua Wang,<sup>b</sup> Delin Chu,<sup>b</sup> Jinhong Yang,<sup>b</sup> Miao Zhang,<sup>a</sup> Jianguo Lv,<sup>d</sup> Baoming Wang,<sup>b</sup> Gang He<sup>a</sup> and Zhaoqi Sun<sup>\*a</sup>

Single crystal  $\text{TiO}_2$  nanosheet array films with dominant  $\{001\}$  facets were synthesized on FTO by a hydrothermal method. A simple strategy for the selective deposition of CdS nanoparticles on the low energy  $\{101\}$  facets by controlling the F content on the surface of  $\text{TiO}_2$  nanosheets is developed. For  $\text{CdS}/\text{TiO}_2$ , under light irradiation, the photo-generated electrons flow from the  $\{001\}$  to  $\{101\}$  facets; meanwhile, the photo-generated electrons transfer from the CdS nanoparticles to the  $\text{TiO}_2$  nanosheets. The deposition of CdS nanoparticles on the  $\{101\}$  facets will shorten the pathways that the electrons must travel. Herein, the synergistic effect of the selective deposition of CdS nanoparticles on the  $\{101\}$  facets of  $\text{TiO}_2$  nanosheets and the different band edge positions of the  $\{001\}$  and  $\{101\}$  facets would facilitate the spatial separation of electrons and holes on different facets, leading to enhanced photoelectronic performance.

Received 26th September 2015,  
Accepted 5th December 2015

DOI: 10.1039/c5ce01905b

[www.rsc.org/crystengcomm](http://www.rsc.org/crystengcomm)

### 1. Introduction

Recently, a series of research groups have focused on the high energy  $\{001\}$  facet of anatase  $\text{TiO}_2$  in order to accomplish efficient solar energy conversion and photocatalysis,<sup>1–4</sup> since Yang *et al.* reported the preparation of single crystal anatase  $\text{TiO}_2$  nanosheets (TNS) with 47% exposed  $\{001\}$  facets.<sup>5</sup> In particular, single crystal anatase TNS grown directly on conducting substrates attract more attention,<sup>6–8</sup> because not only could they obviously reduce inner defects and grain boundaries compared with polycrystal films, but each nanosheet also comes into contact with the conductive substrate independently and provides a direct pathway for charge transport.<sup>9</sup> However, due to their low absorption of solar light and fast recombination of photo-generated electron-hole pairs, the solar energy conversion of TNS is generally retarded. To solve this problem, a variety of strategies including doping of transition metals,<sup>10,11</sup> noble metals<sup>12–14</sup> and semiconductors<sup>15–18</sup> have been developed.

Based on the spatial separation of reduction and oxidation sites on different facets of  $\text{TiO}_2$ , Ohno *et al.* observed the selective deposition of Pt and  $\text{PbO}_2$  on rutile  $\{110\}$  and  $\{011\}$

facets.<sup>19</sup> Liu *et al.* reported the selective deposition of Pt on  $\{101\}$  facets of anatase crystals showing higher photocatalytic hydrogen evolution.<sup>20</sup> Besides, Ohno *et al.* also carried out the selective deposition of Pt nanoparticles on the inner surface of  $\text{TiO}_2$  nanotubes by washing with deionized water and found that the active sites on the outer surface of the  $\text{TiO}_2$  nanotubes were not covered by Pt nanoparticles, resulting in an increase in its photocatalytic activity.<sup>21</sup> For anatase  $\text{TiO}_2$ , it was proposed that the  $\{001\}$  facets show a higher surface energy than the  $\{101\}$  facets,<sup>5,22–24</sup> and their high surface energies induce high surface activities, which will make a stable combination with foreign atoms.<sup>25</sup> Zhang *et al.* prepared  $\text{TiO}_2$  single crystals with high energy  $\{001\}$  and  $\{110\}$  facets. They found that the density of Au particles on the  $\{110\}$  and  $\{001\}$  facets is larger than that on  $\{101\}$  facets, which would promote the separation of electron-hole pairs.<sup>26</sup> Liu *et al.* have synthesized CdS quantum dot-decorated  $\text{TiO}_2$  nanocrystals with stepped  $\{101\}$  surfaces and observed high hydrogen production rates under visible light irradiation.<sup>27</sup> Although many research studies have been made on selective deposition, there are few reports on the selective deposition of CdS nanoparticles on low energy  $\{101\}$  facets of single crystal TNS films.

In this study, TNS films were fabricated by a simple hydrothermal method. Selective deposition of CdS nanoparticles on the  $\{101\}$  facets of TNS films was performed by controlling the F content on the surface of TNS. Their enhanced photoelectronic properties and the probable reasons were discussed. In

<sup>a</sup> School of Physics & Material Science, Anhui University, Hefei 230601, PR China.  
E-mail: szq@ahu.edu.cn

<sup>b</sup> Army Officer Academy, Hefei 230031, PR China

<sup>c</sup> Hefei University of Technology, Hefei 230009, PR China

<sup>d</sup> School of Electronic & Information Engineering, Hefei Normal University, Hefei 230601, PR China

addition, a model for charge separation among different crystal faces and CdS particles was proposed.

## 2. Experimental

### 2.1 Preparation of CdS/TNS films

All major chemicals were of analytical grade and were used as-received without further purification. TNS films were fabricated by a hydrothermal method similar to the method described by Zheng *et al.*<sup>28</sup> 0.5 mL of tetrabutyl titanate was mixed with 30 mL of hydrochloric acid aqueous solution (5.2 M). The mixture was stirred for 10 min before 0.25 g of ammonium hexafluorotitanate was added to the solution, and stirred again for another 30 min. Then, the solution was transferred into a Teflon-lined cylindrical autoclave in which a piece of fluorine-doped tin oxide (FTO) with the conductive side is face up. The Teflon-lined autoclave was kept at 170 °C for 16 h. After cooling down to room temperature, the FTO substrates were taken out and rinsed with deionized water thoroughly and then dried at 80 °C.

Selective deposition of CdS nanoparticles on the TNS films was performed by the successive ion-layer adsorption and reaction (SILAR) approach. In a typical procedure, TNS films were sequentially immersed in two different aqueous solutions for 5 min, first in 0.5 M cadmium nitrate ( $\text{Cd}(\text{NO}_3)_2$ ) and then in 0.5 M sodium sulfide ( $\text{Na}_2\text{S}$ ). Between each immersion step, the films were rinsed with deionized (DI) water to remove the excess ions and dried under a stream of nitrogen. This SILAR operation was repeated 3, 5, 7 and 9 times, and the resulting products were denoted as CdS/TNS-3, CdS/TNS-5, CdS/TNS-7 and CdS/TNS-9, respectively.

### 2.2 Characterization

The crystal structure of the CdS/TNS films was checked by means of X-ray diffraction (XRD, MAC, M18XHF). Their morphology was characterized by scanning electron microscopy (FE-SEM, Hitachi, S4800) and high-resolution transmission electron microscopy (HRTEM, JEM-2100). X-ray photoelectron spectroscopy (XPS, Thermo, ESCALAB 250) was employed to analyze the elemental chemical states and surface compositions of the samples. The amount of CdS in the prepared samples was measured by using an inductively coupled plasma atomic emission spectrometer (ICP-AES, IRIS Intrepid II XSP, Thermo Elemental). The absorbance spectra of the samples were obtained with an ultraviolet-visible spectrophotometer (UV-2550, Shimadzu). Photoluminescence (PL) spectra were measured by using a fluorescence spectrophotometer (FL, Hitachi F-4500) at the excitation wavelength of 325 nm under ambient conditions.

### 2.3 Photoelectronic performance measurements

Photoelectronic performance was measured on an electrochemical workstation (CHI600D) in a photoelectrochemical cell under intermittent AM 1.5G simulated sunlight illumination with 0 V bias potential in 0.1 M  $\text{Na}_2\text{SO}_4$  aqueous

solution. In this system, Ag/AgCl (saturated with KCl), a Pt foil and CdS/TNS films were used as the reference, counter and working electrodes, respectively. The distance between the sample and the counter electrode was 2 cm.

## 3. Results and discussion

### 3.1 XRD patterns

The experimental XRD patterns are shown in Fig. 1. The main characteristic peaks can be indexed to pure anatase phase (JCPDS no. 21-1272). Unlike the conventional method for preparing  $\text{TiO}_2$ ,<sup>29,30</sup> the (004) diffraction peak here is significantly enhanced, indicating the exposure of a large percentage of {001} facets.<sup>28</sup> Compared with the obvious anatase phase, the diffraction peaks of CdS were not easily observed, implying its low content and the small size of CdS species.<sup>31,32</sup> For CdS/TNS-9, one can see that the diffraction peak at 26.5° is slightly intensified. It could be ascribed that the characteristic peak corresponding to the (002) plane of CdS (JCPDS no. 41-1049) was obscured by the FTO peak.

### 3.2 Morphology analysis

Fig. 2(a) and (b) show the top view and cross-sectional view SEM images of a typical as-synthesized TNS on the FTO substrate. Dense regular nanosheets with a side length of ~2 μm and a thickness of ~250 nm tend to grow vertically or obliquely on the FTO substrate. Fig. 2(c)–(f) show the magnified images of CdS/TNS-3, CdS/TNS-5, CdS/TNS-7 and CdS/TNS-9, respectively. From the symmetry of the well-faceted crystal structure of TNS, the two flat square surfaces are identified as {001} facets, while the other lateral surfaces are {101} facets. With an increase in the number of deposition cycles, the surfaces of TNS become rough gradually. It is interesting to note that the CdS nanoparticles are mostly selectively deposited on the {101} facets of anatase TNS. As shown in Fig. 2(c), a small amount of CdS nanoparticles is

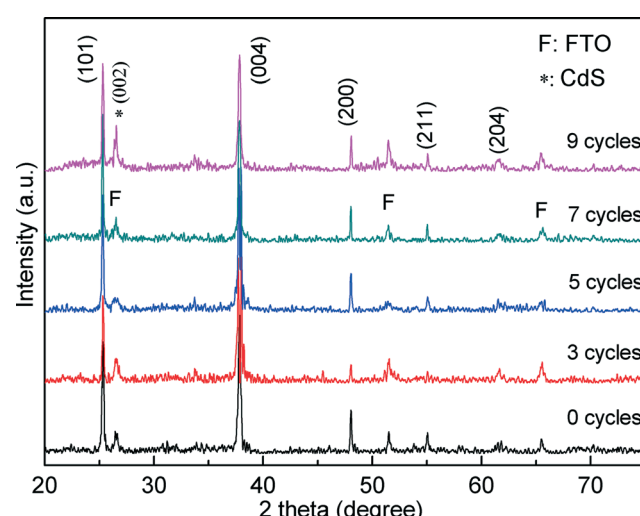
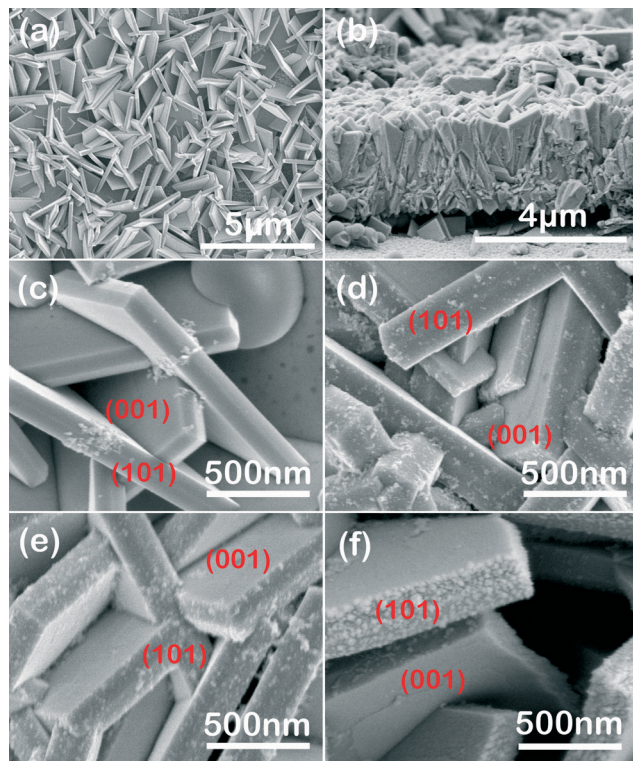


Fig. 1 XRD patterns of CdS/TNS prepared with different SILAR cycles.



**Fig. 2** SEM images of CdS/TNS prepared with different SILAR cycles: (a) 0 cycles, (c) 3 cycles, (d) 5 cycles, (e) 7 cycles and (f) 9 cycles, and (b) a cross-section view.

deposited on the {101} facets of TNS after 3 deposition cycles. After 5 cycles, the amount of CdS nanoparticles increases obviously, with good dispersion on the {101} facets. After 7 cycles, more CdS nanoparticles are deposited on the {101} facets and agglomerate into larger particles. As shown in Table 1, the mean size of the CdS nanoparticles decreases from 15.5 to 9.6 nm as the deposition cycles increase from 3 to 5 times, while with an increase in the number of deposition cycles from 5 to 9, the mean size of the CdS nanoparticles increases from 9.6 to 26.3 nm. As reported by Kamat *et al.*,<sup>33</sup> there are two types of growth of CdS nanocrystals with increasing deposition cycles. One is the formation of new crystallites, while the other is the growth of smaller crystallites into larger crystallites. As the deposition cycles increase to 5, it seems that the first type of growth holds the dominant position. After 5 deposition cycles, CdS crystallites grow into larger crystallites, resulting in the increase in mean size of the CdS nanoparticles.

**Table 1** Mean size of CdS particles and optical band gap of the samples

Cycling times	Mean size of CdS particles (nm)	Optical band gap (eV)
0	—	3.21
3	15.5	3.19
5	9.6	3.19
7	22.6	3.18
9	26.3	3.16

Previously, it was proposed that for anatase single crystals, the {001} facets show a higher surface energy than the {101} facets. Their high surface energy induces high surface activity, which will make a strong combination with foreign atoms such as CdS. In our experiment, CdS is selectively deposited on the {101} facets of the samples, which might be due to the fact that the {001} and {101} facets were terminated by fluorine anions. For F-adsorbed surfaces, the {001} facets become more stable than the {101} facets.<sup>5,34</sup> To elucidate the role of fluorine anions in affecting the deposition of CdS, before deposition of CdS, a TNS film was annealed at 500 °C for 2 h, and then prepared with 5 deposition cycles. From Fig. 3(b), it is worthwhile pointing out that the density of CdS particles on the {001} facets of TNS annealed at 500 °C is higher than that on {101} facets. From the EDS spectra, we can see that in addition to the peaks from O, Ti, Cd, F and S, peaks from the C contaminant and FTO substrate are also present. As shown in Fig. 3(c)–(f) and Table 2, the mass percentage of the F element reduces from ~5.7 to ~2.6% after calcination, and this is due to the fact that the adsorbed fluorine ions on the surface of TiO<sub>2</sub> can be removed by calcination.<sup>5</sup> Meanwhile, the mass percentages of the Cd element on the {101} and {001} facets of unannealed TNS are 1.13 and 0.61%, respectively. However, for TNS annealed at 500 °C, the mass percentages of the Cd element on the {101} and {001} facets are 1.29 and 1.77%, respectively. Careful observation of the EDS spectra reveals that the density of CdS nanoparticles loaded on the {101} facets was much higher than that loaded on the {001} facets when their surface adsorbed more F<sup>-</sup> anions. Besides, the density of CdS particles on TNS is obviously higher after calcination. This is because TNS films annealed at 500 °C have a large percentage of {001} facets, which show higher surface energy and surface activity than {101} facets that will make a strong combination with more CdS nanoparticles. In

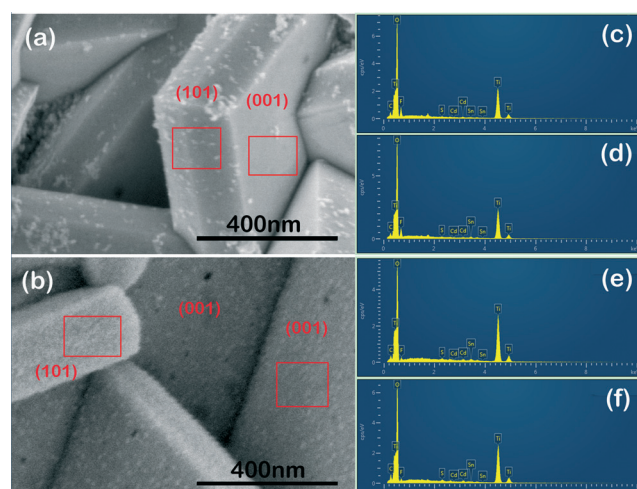


**Fig. 3** The SEM images of CdS-loaded TNS unannealed (a) and annealed at 500 °C for 2 h (b). (c) and (d) The EDS spectra of the (101) and (001) facets for unannealed TNS; (e) and (f) the EDS spectra of the {101} and {001} facets for annealed TNS labelled with block diagrams, respectively.

**Table 2** Elemental content of {101} and {001} facets for CdS/TNS unannealed and annealed at 500 °C

	Unannealed		Annealed	
	Cd (wt%)	F (wt%)	Cd (wt%)	F (wt%)
{101}	1.13	5.76	1.29	2.55
{001}	0.61	5.73	1.77	2.62

addition, the amounts of Cd measured by ICP are 4.10 µg cm<sup>-2</sup> and 5.39 µg cm<sup>-2</sup> for the unannealed and annealed TNS films prepared with 5 deposition cycles.

### 3.3 TEM and HRTEM observation

The TEM image (Fig. 4(a)) of CdS/TNS reveals that the TiO<sub>2</sub> nanosheets are rectangular-shaped structures, and their size is about 2 µm. The selected-area electron diffraction (SAED) pattern of TNS (Fig. 4(b)) can be indexed to the [001] zone axis diffraction, which indicates that the top and bottom surfaces of the TiO<sub>2</sub> nanosheets are highly reactive {001} facets. Fig. 4(c) is the amplified image of the {101} and {001} facets on CdS/TNS. Obviously, after 5 cycles, there are quite a few CdS particles deposited on the {101} facets, while there are fewer on the {001} facets. The HRTEM image in Fig. 4(d) reveals a lattice fringe of about 0.237 nm, which corresponds to the (004) crystal plane of TiO<sub>2</sub>, while  $d = 0.316$  nm corresponds to the (101) crystal plane of CdS, confirming the successful deposition of CdS on the {101} facets of TNS.

### 3.4 XPS analysis

In order to investigate the chemical composition and elemental chemical states, XPS has been carried out for the as-synthesized unannealed and annealed at 500 °C TNS samples

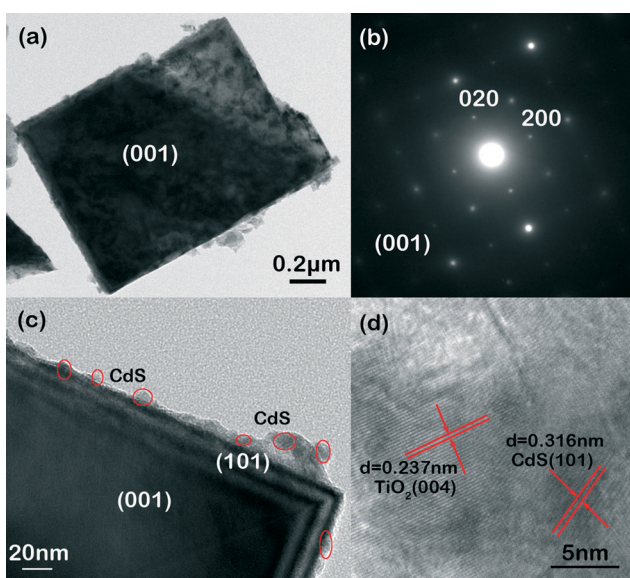


**Fig. 4** (a), (c) TEM images and (d) HRTEM image of CdS/TNS. (b) SAED pattern of the anatase single crystal nanosheet.

with 5 deposition cycles. Fig. 5(a) shows the comparison of the survey spectra of CdS/TNS. Sharp photoelectron peaks of Ti 2p, O 1s, Cd 3d and S 2p appear in both cases, along with a C 1s peak at 284.8 eV due to the adventitious hydrocarbon contaminants or residual elements from the precursor solution. Fig. 5(b) shows the comparison of the high-resolution XPS spectra of F 1s before and after annealing. As is reported, the F 1s peak at 684.5 eV originates from surface fluoride (Ti-F) formed by ligand exchange between F<sup>-</sup> and surface -OH.<sup>35</sup> It is apparent that the surface fluoride of anatase single crystals can be removed by the annealing method.<sup>5</sup> No signal at the binding energy of 688.5 eV for F<sup>-</sup> in the lattice of TiO<sub>2</sub> is found. Fig. 5(c) shows the O 1s core level spectra which can be divided into three different peaks with binding energies of about 529.9, 531.5 and 532.6 eV. The main peak at 529.9 eV is attributed to Ti-O in TiO<sub>2</sub> and the second peak can be assigned to -OH on the surface of TiO<sub>2</sub>.<sup>36</sup> Generally, the peak with the binding energy of about 532.6 eV is attributed to chemisorbed oxygen or organic carbon contaminants containing C-O species.<sup>37-40</sup> According to the results of curve fitting of the O 1s spectra, the hydroxyl content of the samples decreases from 31.6 to 29.9% after annealing, which is due to the dehydration reaction on the surface of the annealed TiO<sub>2</sub>.<sup>41</sup> The S 2p spectra in Fig. 5(e) show obvious peaks at 161.5 and 162.6 eV, corresponding to S 2p<sub>3/2</sub> and S 2p<sub>1/2</sub> of S 2p; the peak at about 169 eV is assigned to the formation of SO<sub>4</sub><sup>2-</sup> or SO<sub>3</sub><sup>2-</sup> species due to the oxidization of sulfide.<sup>42,43</sup> The binding energies of Ti 2p<sub>3/2</sub> and Ti 2p<sub>1/2</sub> are located at 458.7 and 464.5 eV. The peaks of Cd 3d<sub>5/2</sub> and Cd 3d<sub>3/2</sub> at 405.2 and 411.8 eV are all in good agreement with previous studies.<sup>44,45</sup> The atomic ratio of Cd:S is 1.26:1 and 1.13:1 for the samples before and after annealing, which is expected for CdS nanoparticles under normal synthesis conditions.<sup>42,46</sup> In addition, it was found that the peak intensities of Cd 3d increase significantly after calcination, which is in good agreement with the findings of SEM and EDS. Meanwhile, the mean size of CdS nanoparticles in our experiment is approximately 10 nm, which is slightly larger than the depth that XPS could detect; thus, the decrease in peak intensities of Ti 2p can be attributed to the increase in CdS surface coverage.

### 3.5 UV-visible absorption spectra

Fig. 6 presents the typical absorption spectra of TNS films with different SILAR cycles. As is shown, with an increase in the number of deposition cycles, the absorbance increases in the wavelength range from 400 to 500 nm. This can be attributed to the increase in the amount of CdS, which has a band gap of about 2.4 eV.<sup>47</sup> Based on the UV-visible absorption spectra, the  $(\alpha h\nu)^2$  vs. photon energy plots and band gap of the films are shown in Fig. 7 and Table 1. It can be seen that the absorption bands of CdS/TNS show little variation, which change from 3.21 to 3.16 eV. As reported by Zhang,<sup>46</sup> with an increase in the number of deposition cycles from 0 to 5, the band gap of CdS-sensitized TiO<sub>2</sub> nanotube arrays shifts from

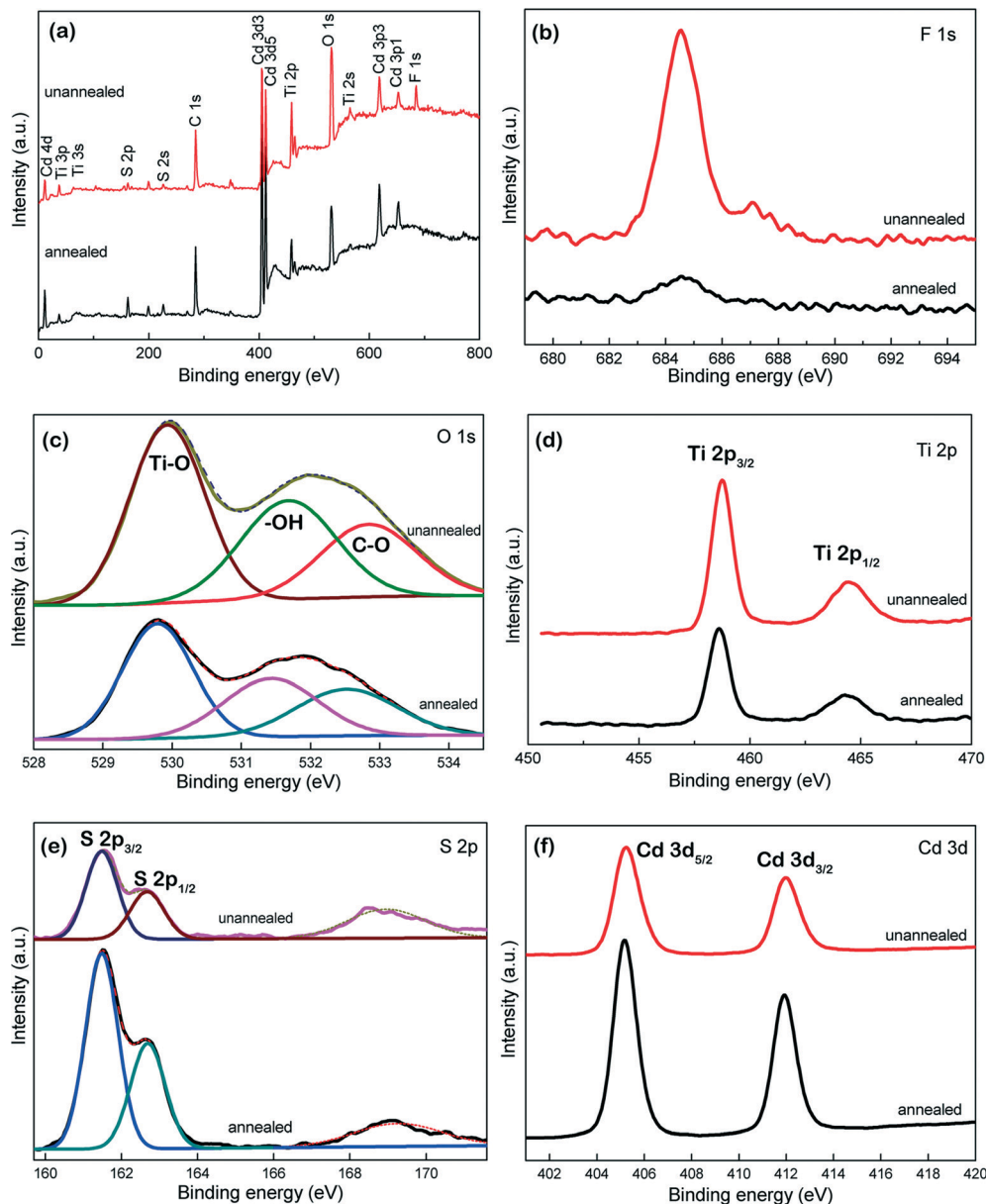


**Fig. 5** (a) Survey, (b) F 1s, (c) O 1s, (d) Ti 2p, (e) S 2p and (f) Cd 3d XPS spectra of CdS/TNS unannealed and annealed at 500 °C for 2 h.

3.09 to 2.81 eV. Hu *et al.* reported that the absorption edge of the CdS-sensitized TiO<sub>2</sub> nanorods shifts from 3.26 to 2.41 eV.<sup>48</sup> In our case, the CdS nanoparticles are mostly selectively deposited on the {101} facets of TNS, resulting in a low CdS content and little change in absorption bands.

### 3.6 PL spectra

For semiconductors, the PL spectrum is related to the trapping, migration and transfer of photo-induced electrons and holes, thus it can reflect the separation and recombination of photo-induced charge carriers.<sup>49,50</sup> The PL spectra of TNS prepared with different SILAR cycles were obtained by using an excitation wavelength of 325 nm at room temperature. As shown in Fig. 8, three main peaks can be observed, which

are situated at 397, 452 and 469 nm. The first peak is ascribed to the emission of band gap transition.<sup>51</sup> The emission peaks at 452 and 469 nm result from the oxygen defects, which are related to the charge-transfer transition from Ti<sup>3+</sup> to the oxygen anion in a TiO<sub>6</sub><sup>8-</sup> complex.<sup>51,52</sup> Compared with bare TNS, the PL intensities of CdS/TNS significantly decrease, indicating that CdS/TNS has a lower recombination rate of photo-induced charge carriers. Observation of the PL spectra reveals that the PL intensity of CdS/TNS decreases with an increase in the number of deposition cycles from 3 to 7, indicating that the more CdS nanocrystallites are deposited on the {101} facets of TNS, the slower the electron–hole pair recombination is. For CdS/TNS-9, the increase in PL intensity could be attributed to the aggregation of CdS nanoparticles. Furthermore, the intensity ratio of the band edge

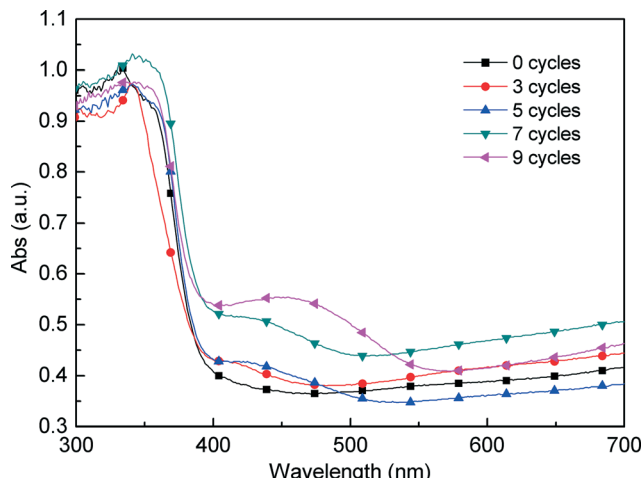


Fig. 6 UV-Visible absorption spectra of CdS/TNS prepared with different SILAR cycles.

emission to visible emission decreases with an increase in the number of SILAR cycles, indicating that the oxygen defects of CdS/TNS increase when more CdS nanocrystallites are deposited on TNS.<sup>53</sup>

### 3.7 Transient photocurrent response

Fig. 9 shows the time-dependent photocurrent curves of CdS/TNS under intermittent AM 1.5G simulated sunlight illumination. As is shown, the photocurrents increase with more SILAR cycles. After 7 cycles, the sample shows the highest photocurrent value of  $\sim 60 \mu\text{A cm}^{-2}$ , which is about 10 times higher than that for pristine TNS; nevertheless, it decreases

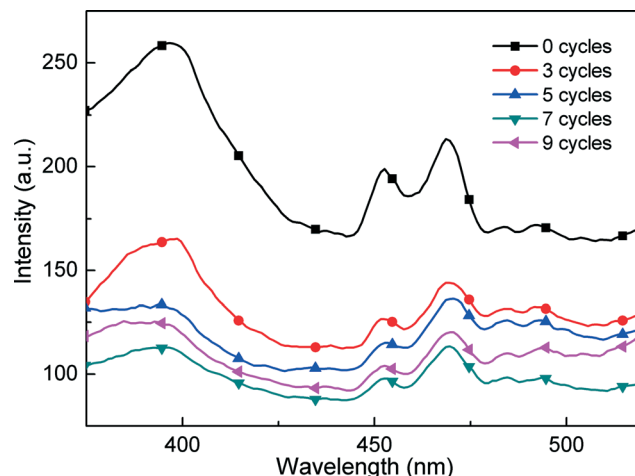


Fig. 8 PL spectra of CdS/TNS prepared with different SILAR cycles.

as the deposition cycles increase to 9 times. The increase in photocurrent may be attributed to the fact that CdS is a narrow band gap semiconductor, which would enhance the absorption of visible light. When the deposition cycles further increase to 9 times, the aggregation of CdS covering the {101} facets of CdS/TNS-9 leads to the formation of larger CdS particles. These large CdS particles might reduce the electron transfer rate.<sup>54</sup> Besides, the grain boundaries and defects among excess CdS nanoparticles can act as recombination centers of charge carriers, which will result in the decrease in photoelectric performance.<sup>9</sup> Furthermore, from the SEM images, it can be seen that the {101} facets of CdS/TNS-9 are covered with CdS particles completely, which may inhibit the

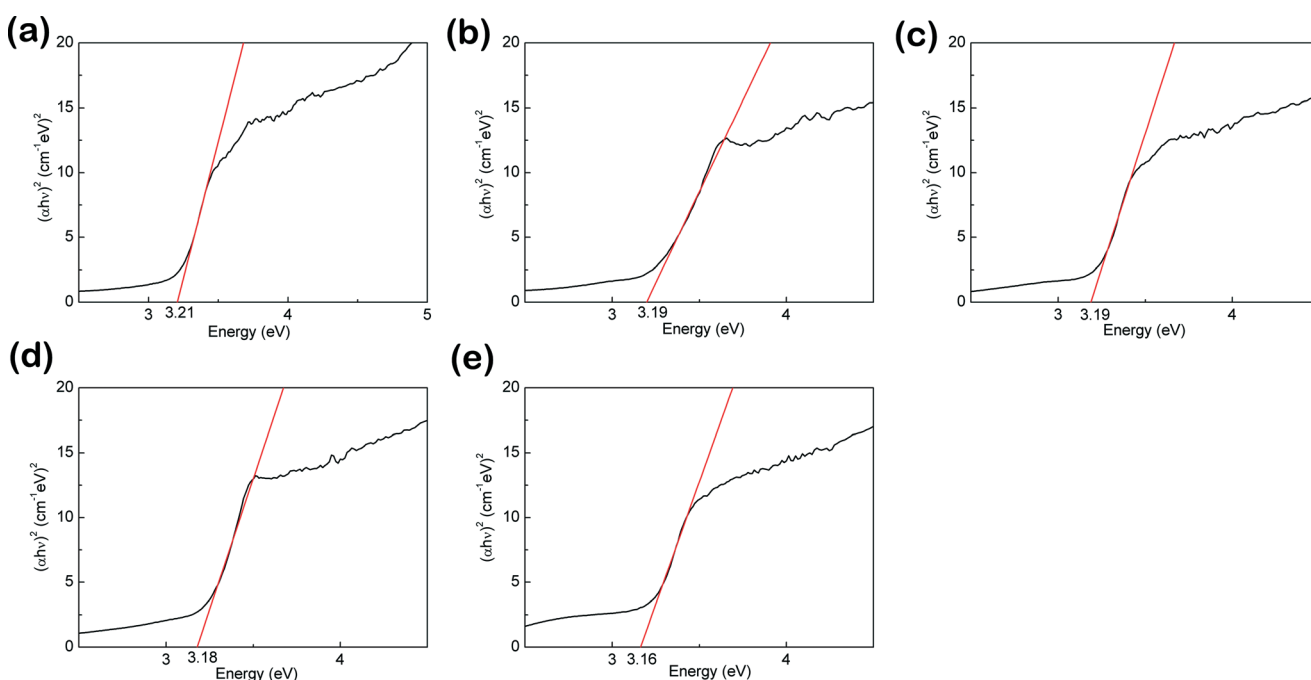


Fig. 7 Plots of  $(\alpha h\nu)^2$  vs. photon energy for CdS/TNS prepared with different SILAR cycles: (a) 0 cycles, (b) 3 cycles, (c) 5 cycles, (d) 7 cycles and (e) 9 cycles.

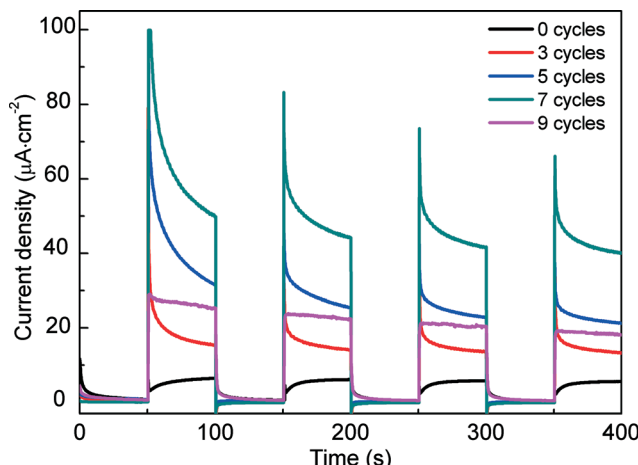


Fig. 9 Transient photocurrents of CdS/TNS prepared with different SILAR cycles.

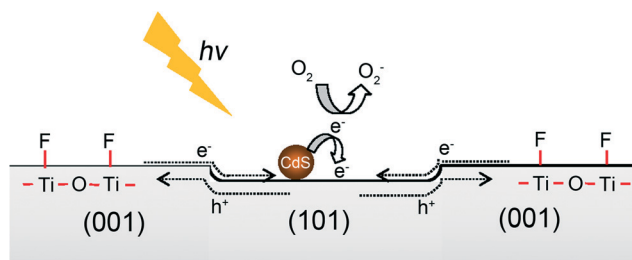


Fig. 10 Schematic diagram of charge separation among different crystal faces and CdS particles.

transfer of photoexcited electrons from the  $\{001\}$  facet to the  $\{101\}$  facet, resulting in the reduced photocurrent.

Fig. 10 shows the schematic diagram of charge separation among different crystal faces and CdS particles. For F-adsorbed surfaces, it was proposed that the Ti-F bonds are stronger in the  $\{001\}$  facets than those in the  $\{101\}$  facets, which induces the surface energy of  $\{001\}$  facets to be lower than that of  $\{101\}$  facets.<sup>5</sup> Recently, Ma *et al.* reported that the Ti-O bonds are weakened in the F-adsorbed  $\{101\}$  facets while they are strengthened in the  $\{001\}$  facets, thus the  $\{101\}$  facets become more active than the  $\{001\}$  facets, which will facilitate a strong combination with foreign atoms such as CdS.<sup>34</sup> Under light irradiation, the photo-excited electrons from CdS can easily transfer to the  $\{101\}$  facets of TNS, due to the high crystallinity of TNS and the favorable energy level between CdS and  $\text{TiO}_2$ , thus preventing the recombination of electron-hole pairs.<sup>55</sup> Due to the atomic arrangement characteristics, different crystal faces possess different surface band structures and band edge positions.<sup>56</sup> For anatase  $\text{TiO}_2$ , Ohno *et al.* found that the reduction and oxidation sites are located on  $\{101\}$  and  $\{001\}$  facets, respectively.<sup>57</sup> By means of single-molecule fluorescence spectroscopy, Tachikawa *et al.* demonstrated the electron flow from the  $\{001\}$  to  $\{101\}$  facets.<sup>58</sup> Based on density functional theory calculations, Yu *et al.* proposed a “surface heterojunction” concept to explain the

difference in the photocatalytic activities of  $\text{TiO}_2$  with co-exposed  $\{001\}$  and  $\{101\}$  facets.<sup>59</sup> When CdS is combined with  $\text{TiO}_2$ , local band bending occurs at the CdS/ $\text{TiO}_2$  interface. Under light irradiation, CdS effectively excites electron-hole pairs. The excited electrons can quickly transfer from the CdS conduction band to the TNS. Due to the convergence of electrons on  $\{101\}$  facets, the deposition of CdS particles on the  $\{101\}$  facets will shorten the pathways that the electrons must travel, hence enabling the improvement of the separation of electrons and holes. Herein, the enhanced photoelectronic performance of CdS/TNS can be attributed to the synergistic effect of the selective deposition of CdS nanoparticles on the  $\{101\}$  facets of  $\text{TiO}_2$  nanosheets and the different band edge positions of  $\{001\}$  and  $\{101\}$  facets, which would facilitate the spatial separation of electrons and holes on different facets and retard the recombination of light-generated electron-hole pairs.

## 4. Conclusions

In summary, we have developed a simple strategy for the selective deposition of CdS particles on  $\{101\}$  facets by controlling the F content on the surface of TNS. For anatase single crystals, the electrons flow from  $\{001\}$  to  $\{101\}$  facets and the deposition of CdS nanoparticles on the  $\{101\}$  facets will shorten the pathways that the electrons must travel, hence enabling the improvement of the separation of electrons and holes. The finding of this work provides a new way to improve photoelectronic performance through deposition of foreign atoms on low energy surfaces.

## Acknowledgements

This work is supported by the National Natural Science Foundation of China (No. 51472003 and 51272001) and the National Key Basic Research Program (2013CB632705). The authors would like to thank Yonglong Zhuang and Zhongqing Lin of the Experimental Technology Center of Anhui University for the electron microscopy test and discussion.

## References

- B. Banerjee, V. Amoli, A. Maurya, A. K. Sinha and A. Bhaumik, *Nanoscale*, 2015, 7, 10504–10512.
- F. Wang, S. Zhang, C. Li, J. Liu, S. He, Y. Zhao, H. Yan, M. Wei, D. G. Evans and X. Duan, *RSC Adv.*, 2014, 4, 10834–10840.
- B. Wang, X.-Y. Lu, L. K. Yu, J. Xuan, M. K. H. Leung and H. Guo, *CrystEngComm*, 2014, 16, 10046–10055.
- Q. Shi, Y. Li, E. Zhan, N. Ta and W. Shen, *CrystEngComm*, 2015, 17, 3376–3382.
- H. G. Yang, C. H. Sun, S. Z. Qiao, J. Zou, G. Liu, S. C. Smith, H. M. Cheng and G. Q. Lu, *Nature*, 2008, 453, 638–641.
- F. Li, X. Li, R. Peng, X. Zhai, S. Yang, Z. Fu and Y. Lu, *Nanoscale*, 2014, 6, 12434–12439.

- 7 B. Liu and E. S. Aydil, *Chem. Commun.*, 2011, **47**, 9507–9509.
- 8 T. K. Van, C. K. Nguyen and Y. S. Kang, *Chem. – Eur. J.*, 2013, **19**, 9376–9380.
- 9 M. Zhou, X. W. D. Lou and Y. Xie, *Nano Today*, 2013, **8**, 598–618.
- 10 M. Anpo and M. Takeuchi, *J. Catal.*, 2003, **216**, 505–516.
- 11 J. Choi, H. Park and M. R. Hoffmann, *J. Phys. Chem. C*, 2009, **114**, 783–792.
- 12 S. Zhu, S. Liang, Q. Gu, L. Xie, J. Wang, Z. Ding and P. Liu, *Appl. Catal., B*, 2012, **119**, 146–155.
- 13 X.-F. Wu, Y.-F. Chen, J.-M. Yoon and Y.-T. Yu, *Mater. Lett.*, 2010, **64**, 2208–2210.
- 14 D. Yang, N. Yang and J. Ge, *CrystEngComm*, 2013, **15**, 7230–7235.
- 15 J. Hou, C. Yang, Z. Wang, S. Jiao and H. Zhu, *Appl. Catal., B*, 2013, **129**, 333–341.
- 16 S. Lee, K. Lee, W. D. Kim, S. Lee, D. J. Shin and D. C. Lee, *J. Phys. Chem. C*, 2014, **118**, 23627–23634.
- 17 X. Li, X. Chen, H. Niu, X. Han, T. Zhang, J. Liu, H. Lin and F. Qu, *J. Colloid Interface Sci.*, 2015, **452**, 89–97.
- 18 Y. Zhu, R. Wang, W. Zhang, H. Ge and L. Li, *Appl. Surf. Sci.*, 2014, **315**, 149–153.
- 19 T. Ohno, K. Sarukawa and M. Matsumura, *New J. Chem.*, 2002, **26**, 1167–1170.
- 20 C. Liu, X. Han, S. Xie, Q. Kuang, X. Wang, M. Jin, Z. Xie and L. Zheng, *Chem. – Asian J.*, 2013, **8**, 282–289.
- 21 K. Nishijima, T. Fukahori, N. Murakami, T.-A. Kamai, T. Tsubota and T. Ohno, *Appl. Catal., A*, 2008, **337**, 105–109.
- 22 U. Diebold, *Surf. Sci. Rep.*, 2003, **48**, 53–229.
- 23 T. Sun, Y. Wang, M. Al-Mamun, H. Zhang, P. Liu and H. Zhao, *RSC Adv.*, 2015, **5**, 12860–12865.
- 24 C. Li, C. Koenigsmann, W. Ding, B. Rudshteyn, K. R. Yang, K. P. Regan, S. J. Konezny, V. S. Batista, G. W. Brudvig, C. A. Schmuttenmaer and J.-H. Kim, *J. Am. Chem. Soc.*, 2015, **137**, 1520–1529.
- 25 D. He, M. Chen, F. Teng, G. Li, H. Shi, J. Wang, M. Xu, T. Lu, X. Ji, Y. Lv and Y. Zhu, *Superlattices Microstruct.*, 2012, **51**, 799–808.
- 26 M.-Y. Xing, B.-X. Yang, H. Yu, B.-Z. Tian, S. Bagwasi, J.-L. Zhang and X.-Q. Gong, *J. Phys. Chem. Lett.*, 2013, **4**, 3910–3917.
- 27 X. Yao, T. Liu, X. Liu and L. Lu, *Chem. Eng. J.*, 2014, **255**, 28–39.
- 28 Z. Zheng, W. Xie, Z. S. Lim, L. You and J. Wang, *Sci. Rep.*, 2014, **4**.
- 29 Y. Xu, M. Zhang, M. Zhang, J. Lv, X. Jiang, G. He, X. Song and Z. Sun, *Appl. Surf. Sci.*, 2014, **315**, 299–306.
- 30 F. Meng, X. Song and Z. Sun, *Vacuum*, 2009, **83**, 1147–1151.
- 31 Z. Bian, J. Zhu, S. Wang, Y. Cao, X. Qian and H. Li, *J. Phys. Chem. C*, 2008, **112**, 6258–6262.
- 32 Y. Yang, J. Wen, J. Wei, R. Xiong, J. Shi and C. Pan, *ACS Appl. Mater. Interfaces*, 2013, **5**, 6201–6207.
- 33 D. R. Baker and P. V. Kamat, *Adv. Funct. Mater.*, 2009, **19**, 805–811.
- 34 X. Ma, Y. Dai, W. Wei, B. Huang and M.-H. Whangbo, *J. Phys. Chem. Lett.*, 2015, **6**, 1876–1882.
- 35 K. Lv, Q. Xiang and J. Yu, *Appl. Catal., B*, 2011, **104**, 275–281.
- 36 B. Gao, X. Yuan, P. Lu, B. Lin and Y. Chen, *J. Phys. Chem. Solids*, 2015, **87**, 171–176.
- 37 E. McCafferty and J. P. Wightman, *Surf. Interface Anal.*, 1998, **26**, 549–564.
- 38 H. Liu, W. Yang, Y. Ma, Y. Cao, J. Yao, J. Zhang and T. Hu, *Langmuir*, 2003, **19**, 3001–3005.
- 39 N. Kruse and S. Chenakin, *Appl. Catal., A*, 2011, **391**, 367–376.
- 40 M. Zhang, M. Zhang, S. Shi, X. Song and Z. Sun, *J. Alloys Compd.*, 2014, **591**, 213–217.
- 41 J. Yu, G. Dai and B. Cheng, *J. Phys. Chem. C*, 2010, **114**, 19378–19385.
- 42 S. Chen, P. Maggie, R. Chuanmin, G. K. Mor, O. K. Varghese, K. Dimitris and C. A. Grimes, *J. Photochem. Photobiol., A*, 2006, **177**, 177–184.
- 43 X. Wang, Z. Chen, Y. Luo, L. Jiang and R. Wang, *Sci. Rep.*, 2013, **3**, 449–449.
- 44 S. Yousefzadeh, M. Faraji, Y. T. Nien and A. Z. Moshfegh, *Appl. Surf. Sci.*, 2014, **320**, 772–779.
- 45 Y. Zhu, Y. Wang, Z. Chen, L. Qin, L. Yang, L. Zhu, P. Tang, T. Gao, Y. Huang, Z. Sha and G. Tang, *Appl. Catal., A*, 2015, **498**, 159–166.
- 46 M. Zhang, S. Shi, G. He, X. Song and Z. Sun, *Sci. Adv. Mater.*, 2014, **6**, 171–177.
- 47 N. Qin, Y. Liu, W. Wu, L. Shen, X. Chen, Z. Li and L. Wu, *Langmuir*, 2015, **31**, 1203–1209.
- 48 Y. Hu, B. Wang, J. Zhang, T. Wang, R. Liu, J. Zhang, X. Wang and H. Wang, *Nanoscale Res. Lett.*, 2013, **8**, 222.
- 49 J. Hou, C. Yang, Z. Wang, S. Jiao and H. Zhu, *Appl. Catal., B*, 2013, **129**, 333–341.
- 50 Y. Wang, W. Chu, S. Wang, Z. Li, Y. Zeng, S. Yan and Y. Sun, *ACS Appl. Mater. Interfaces*, 2014, **6**, 20197–20204.
- 51 F. B. Li and X. Z. Li, *Chemosphere*, 2002, **48**, 1103–1111.
- 52 J.-G. Yu, H.-G. Yu, B. Cheng, X.-J. Zhao, J. C. Yu and W.-K. Ho, *J. Phys. Chem. B*, 2003, **107**, 13871–13879.
- 53 J. Lv, W. Gong, K. Huang, J. Zhu, F. Meng, X. Song and Z. Sun, *Superlattices Microstruct.*, 2011, **50**, 98–106.
- 54 G. Hodes, *J. Phys. Chem. C*, 2008, **112**, 17778–17787.
- 55 J. Zhang, F.-X. Xiao, G. Xiao and B. Liu, *New J. Chem.*, 2015, **39**, 279–286.
- 56 E. áToby Kelsey, *J. Mater. Chem.*, 1997, **7**, 563–568.
- 57 N. Murakami, Y. Kurihara, T. Tsubota and T. Ohno, *J. Phys. Chem. C*, 2009, **113**, 3062–3069.
- 58 T. Tachikawa, S. Yamashita and T. Majima, *J. Am. Chem. Soc.*, 2011, **133**, 7197–7204.
- 59 J. Yu, J. Low, W. Xiao, P. Zhou and M. Jaroniec, *J. Am. Chem. Soc.*, 2014, **136**, 8839–8842.